Experimental and Numerical Investigation of a Three-Dimensional Vertical-Axis Wind Turbine with Variable-Pitch

by

M. Elkhoury[‡], T. Kiwata[*], and E. Aoun[+]

Abstract

A combined experimental and numerical investigation is carried out to study the performance of a micro Vertical-Axis Wind Turbine (VAWT) with variable-pitch. Three-dimensional numerical simulations are essentially employed, for the VAWT involves a low Aspect Ratio (AR) three straight blades with struts. The performance of the VAWT is experimentally measured using a wind tunnel, while Large Eddy Simulation (LES) with dynamic Smagorinsky SubGrid Scale (SGS) model is employed to help understand the associated flow structure. The effects of wind speed, turbulence intensity, airfoil shape, and strut mechanism with and without variable-pitch on the performance of the turbine are carefully assessed, both experimentally and numerically. The accuracy of the SGS model in predicting the laminar-turbulent transition is also examined.

Keywords: Vertical-Axis Wind Turbine, Large Eddy Simulation, Variable-Pitch, Wind Tunnel Experiments

1. Introduction

Wind turbines have been historically known to be mounted in open rural areas. However, in recent years, there has been an increasing interest in the deploying these turbine in urban areas. The chief objective is to generate energy on site thereby cutting cables cost and reducing transmission loses [1]. Horizontal Axis Wind Turbines (HAWTs) have long been utilized in large-scale wind farms, for they are known to be more efficient than VAWTs in steady winds. Small scales HAWTs have also been

[‡] Associate Professor of Mechanical Engineering, Lebanese American University, P.O.Box: 36 Byblos, Lebanon; Email: mkhoury@lau.edu.lb

[*] Professor of Mechanical Engineering, Kanazawa University, Kakuma-machi, Kanazawa-shi, Ishikawa 920-1192, Japan; E-mail: kiwata@t.kanazawa-u.ac.jp

[+] Student of Mechanical Engineering, Lebanese American University, P.O.Box: 36 Byblos, Lebanon; Email: elio.aoun@lau.edu.lb

increasingly implemented in built environments. However, various recent studies have shown that VAWTs perform better in urban areas when compare to HAWTs [1-4]. These advantages are mainly due to various reasons, the most important of which is the VAWTs' ability to function in a multidirectional flow of wind that could continuously change in residential areas. Unlike HAWTs, VAWTs do not need a yaw control mechanism and respond instantly to change in wind speed and direction, which in turn makes them more efficient in turbulent flow regions.

In recent decades there has been a substantial increase in the use of Computational Fluid Dynamics (CFD) to depict performance of VAWTs. This has been mainly driven not only by the increase in availability of user-friendly CFD software and relatively affordable computational cost, but also by the complexity of flow structures associated with VAWTs. Performance of a three-blade wind turbine has been recently investigated using 2-D CFD by Dai and Lam [5] who compared results against experimental data at a single TSR value. 2-D CFD simulations were also performed for a straight-bladed darrieus-type cross flow marine turbine by Lain [6] and favorably assessed their findings against experiments of Dai and Lam's [5] however, at a single TSR value. Danao et. al. [7] studied the influence of unsteady incoming wind on the performance of a 2-D VAWT. Mesh independent solution by means of Richardson Extrapolation method, Grid Convergence Index method, and the fitting method, was recently investigated for a 2-D VAWT by Almohammadi, et.al. [8]. Nobile, et. al. [9] carried out a 2-D CFD investigation of an augmented VAWT that involved omnidirectional stator located around the VAWT. They reported an increase of around 30 to 35 % in torque and power coefficients.

Elkhoury et. al. [10] assessed the influence of various turbulence models on the performance of a straight-blade VAWT utilizing a 2-D CFD analysis. With similar experimental and computational setup to the currently considered test cases, overestimations of power coefficients were predicted by fully turbulent models, a scenario that was deemed to be due to laminar-turbulent transition. Lanzafame et. al [11] compared predictions of classical fully turbulence models to those of the SST transition model [12] for a VAWT utilizing a 2D CFD solver. McLaren, et.al. [13] successfully performed a 2D Unsteady Reynolds-Averaged Navier-Stokes (URANS) CFD simulation of a small-scale high solidity wind turbine. Scheurich and Brown [14] used the vorticity transport model to investigate performance and wake dynamics of different VAWT configurations in steady and unsteady wind conditions.

Studies considered previously were all bounded by 2D simulations utilizing 2D flow models, many of which were performed at a specific TSR with scarce experimental data that are essential to validate the models. These recently accomplished studies do not account for connecting rods that tend to have considerable influence on the performance of a VAWT. This important feature cannot be neglected at high TSR [10], not to mention blade-rod interference that arises at low TSR. Furthermore, flow over turbines with low AR blades departs from the 2D behavior as blade tip effects become significant, rendering the flow three-dimensional.

To address these limitations, this work capitalizes on such aspects and aims at building a credible 3D CFD model that closely predicts the experimental results. Within this framework, the effects of incoming freestream velocity, turbulence intensity, fixed- and variable-pitch mechanism, and airfoil shape on the power coefficient of the turbine are carefully assessed. LES is employed as the complexity of the flowfield represented by high solidity and low AR. In addition, the interference among the three blades is substantial and would be affected further by the presence of the central shaft and the connecting four-bar linkage mechanism, necessitating a 3-D modeling approach. Furthermore, the ability of LES with dynamic SGS model to predict separation induced transition associated with dynamic stall at relatively low TSRs is examined. It is worth noting that any future attempt to improve this novel design of VAWTs should be facilitated by the use of 3D CFD simulations.

2. Variable-Pitch Mechanism and Experimental System

A 3-D overview of the wind turbine with a variable-pitch angle mechanism is depicted in Fig.1. The turbine had a diameter of 0.8 m and a height (blade span) of 0.8 m. The turbine had three straight blades each was connected to the rotor's center by three main circular rods with a diameter of 0.02m each. The pitch of the three straight-blade rotor varies by means of a four-bar linkage mechanism, the top view of which is shown in Fig.1 b.
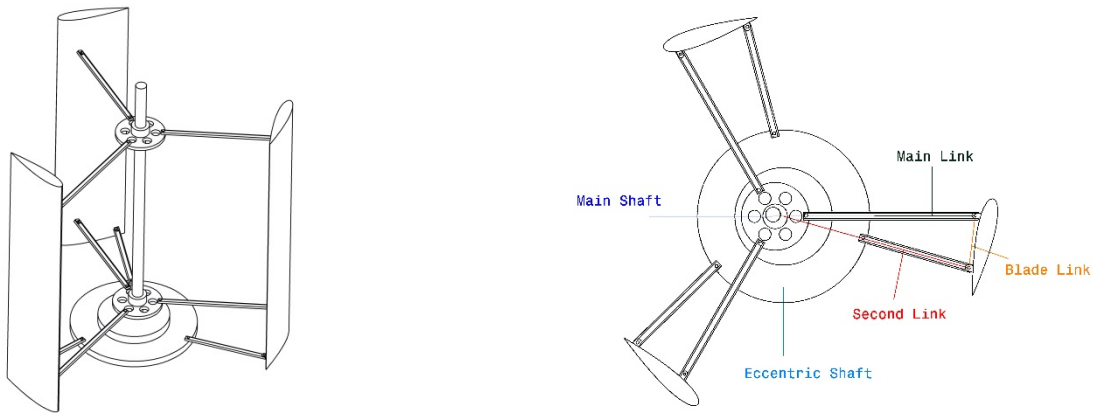
Figure 1: A 3-D overview of the modeled wind turbine a) Isometric view of the rotor b) Top view of the rotor

The pitching axis for the variable-pitch mechanism was located approximately at 15% of the chord from the leading edge. This mechanism has an eccentric rotational center which is different from the main rotational point as shown in Fig. 2. Thus, this mechanism is able to vary blade pitch angle α_p, which is the angle between the blade chord line (i.e., blade-link lc) and a perpendicular line to the main-link, without actuators. This mechanism is able to make an arbitrary selection of the blade offset pitch angle α_c (i.e., an average of the change of blade pitch angle) and the blade pitch angle amplitude α_w by combinations of the link length. The blade offset pitch angle α_c decreases with increasing length of the second link ls. The blade pitch angle amplitude α_w increases with increasing length of the eccentric-link le. The angle between the main link lm and the eccentric link le is the blade azimuth angle ϕ, and θ_p is the angle between the eccentric-link and the wind direction. The average amplitude of the blade angle of attack for $\theta_p =120°$ is larger than that of the wind turbine of fixed-pitch blade while the variation of blade angle of attack for $\theta_p = 0°$ is smaller than that for $\theta_p = 120°$. Therefore, an optimum blade angle of attack could be maintained at all azimuthal angles, improving the performance of the VAWT.
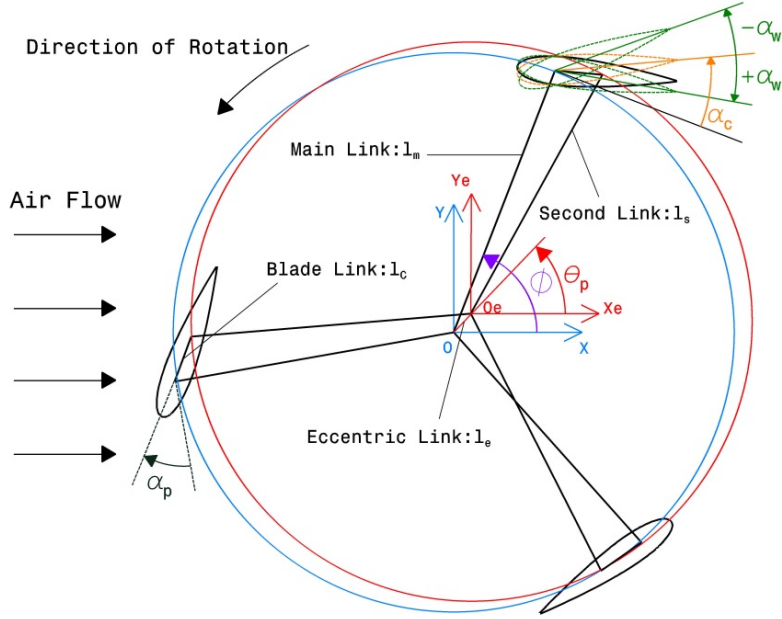
Figure 2: Schematic diagram of the variable-pitch angle mechanism

The equations governing the motion of the pitch-angle in each quadrant are given as follows

$\alpha_p = \pi/2 - (\beta + \gamma)$ for $0 < \varphi < \pi$, and $\alpha_p = \pi/2 - (-\beta + \gamma)$ for $\pi < \varphi < 2\pi$,

where

$$\beta = \cos^{-1}\left(\frac{d^2 + l_m^2 - l_e^2}{2dl_m}\right), \ \gamma = \cos^{-1}\left(\frac{d^2 + l_c^2 - l_s^2}{2dl_c}\right) \tag{1}$$

For $\alpha_p = \pi/2 - \varepsilon$ for $\varphi = 0$, and $\alpha_p = \pi/2 - \delta$ for $\varphi = \pi$

where

$$\varepsilon = \cos^{-1}\left(\frac{l_c^2 + (l_m - l_e)^2 - l_s^2}{2l_c(l_m - l_e)}\right), \delta = \cos^{-1}\left(\frac{l_c^2 + (l_m + l_e)^2 - l_s^2}{2l_c(l_m + l_e)}\right) \tag{2}$$

Experiments were performed in a large-scale open-circuit type wind tunnel, with a square test section of 1.2 m ×1.2 m and a 1.4 m long working section. A schematic diagram of the apparatus is depicted in Fig. 3. The turbulence intensity level and flow non-uniformity at a wind speed of 6 m/s in the working section were less than 0.8% and ±1.8%, respectively. Two freestream velocity values of 6 and 8 m/s were employed corresponding to Reynolds numbers of $Re=8.002\times10^3$ and $Re=1.067\times10^4$, respectively.

The performance of the wind turbine with three different airfoil sections, namely, NACA 0018, NACA63₄-221, and NACA 0012 was measured in the present experiments. All utilized blades had a chord of C=0.2 m and were made of aluminum monocoque with thin wall thickness of 0.5 mm. Table 1 summarizes the considered VAWT specifications.

A three-phase induction motor (Mitsubishi Electric, SB-JR 2.2kW 4P) accompanied by a variable-frequency inverter (Hitachi, SJ200) was used to drive the turbine. Thus the behavior of the power coefficient, C_p, could be easily observed at different TSRs by varying the frequency of the motor. In order to calculate the power coefficient, the torque and rotation speed of the turbine were measured in each case using a torque transducer (TEAC TQ-AR5N with a rated capacity of 5N.m) and a digital tachometer (ONO SOKKI HT-5500). The wind speed in the working section was measured using a Pitot tube and a thermal anemometer (KANOMAX, Climomaster model 6531).

Table 1: Turbine specifications

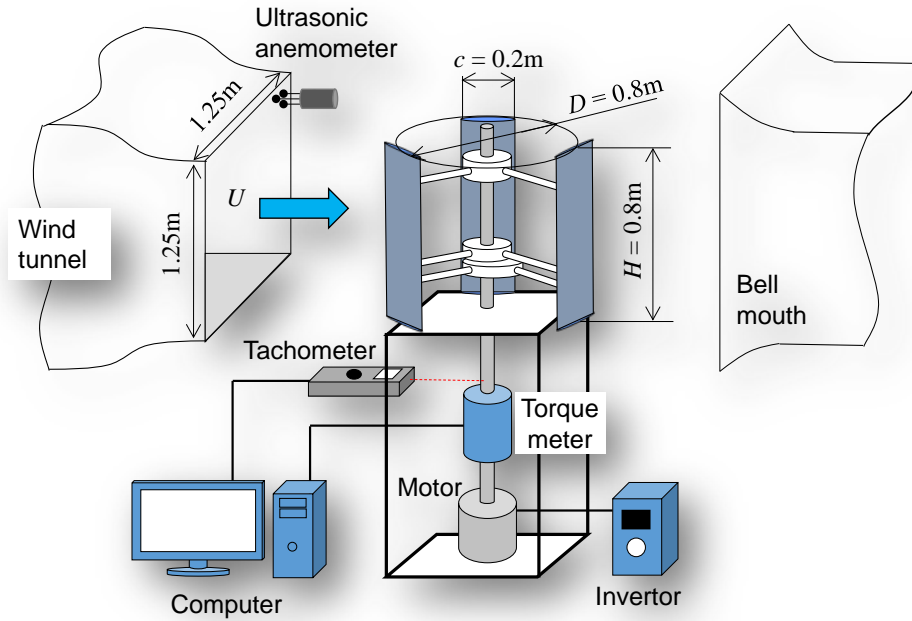| Turbine diameter D	800 mm
Blade span h	800 mm
Blade chord length c	200 mm
Airfoil section	NACA 63₄-221, NACA 0018, NACA 0021
Number of blades N	3
Main-link lm	373 mm
Second-link ls	365 mm
Eccentric-link le	16mm
Blade-link lc	85 mm
Solidity σ	0.75
Aspect Ratio AR	4

Figure 3: Schematic diagram of the experimental apparatus

3. Computational Set-up and Numerical Approach

3.1 Components of Simulated VAWT

Effects of connecting rods cannot be neglected especially for TSRs > 1 [10]. Thus, to account for their influence, it was necessary to undertake a 3-D approach. However, the modeled rotor had simpler mechanisms/connections than that used in the experimental setup. This in turn will substantially improve the mesh quality and as a result accelerate convergence with minimal influence on the accuracy of the results. The modeled rotor had 3 straight blades with matching dimensions to the experimental setup, resulting in an AR of 4. 3-D effects manifested at the blade tip cannot be neglected for such a low AR, creating another incentive for the 3-D approach. The blades were linked to the shaft through 9 straight cylindrical rods; 2 of which support every blade. The rotor's shaft had a diameter of 5cm. The rods on another hand had diameters ranging from 1.0 to 1.5 cm. Finally, the blade was connected to the main crank at 0.25c as was the case in the experiment.

3.2 Computational Domain

The 3-D investigation of the VAWT necessitates the partitioning of the computational domain into three regions: blade domain, rotor domain, and wind tunnel domain. The blade domain is a moving domain, engulfed by the rotor domain which is also rotating. The rotor domain is encapsulated inside the wind tunnel domain as depicted in Fig. 4.
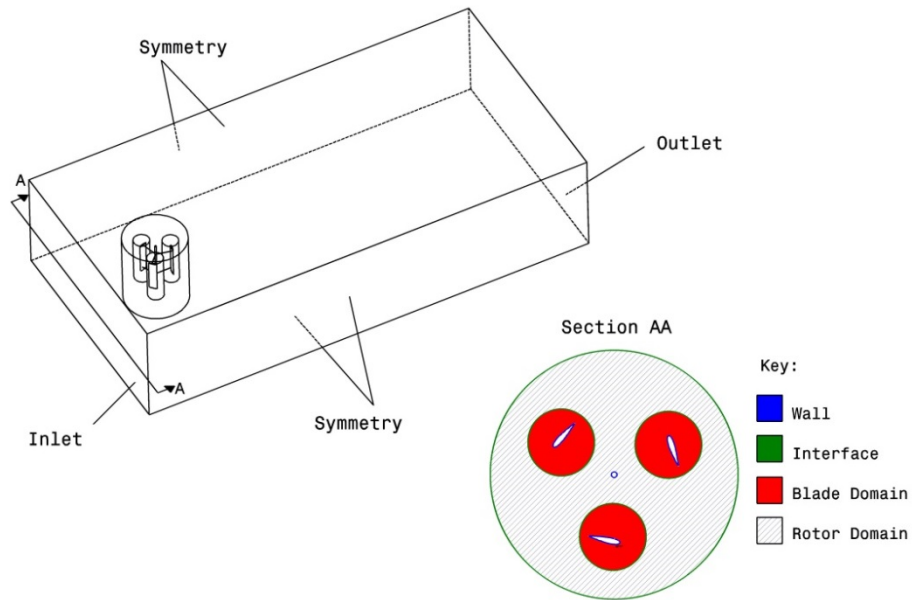

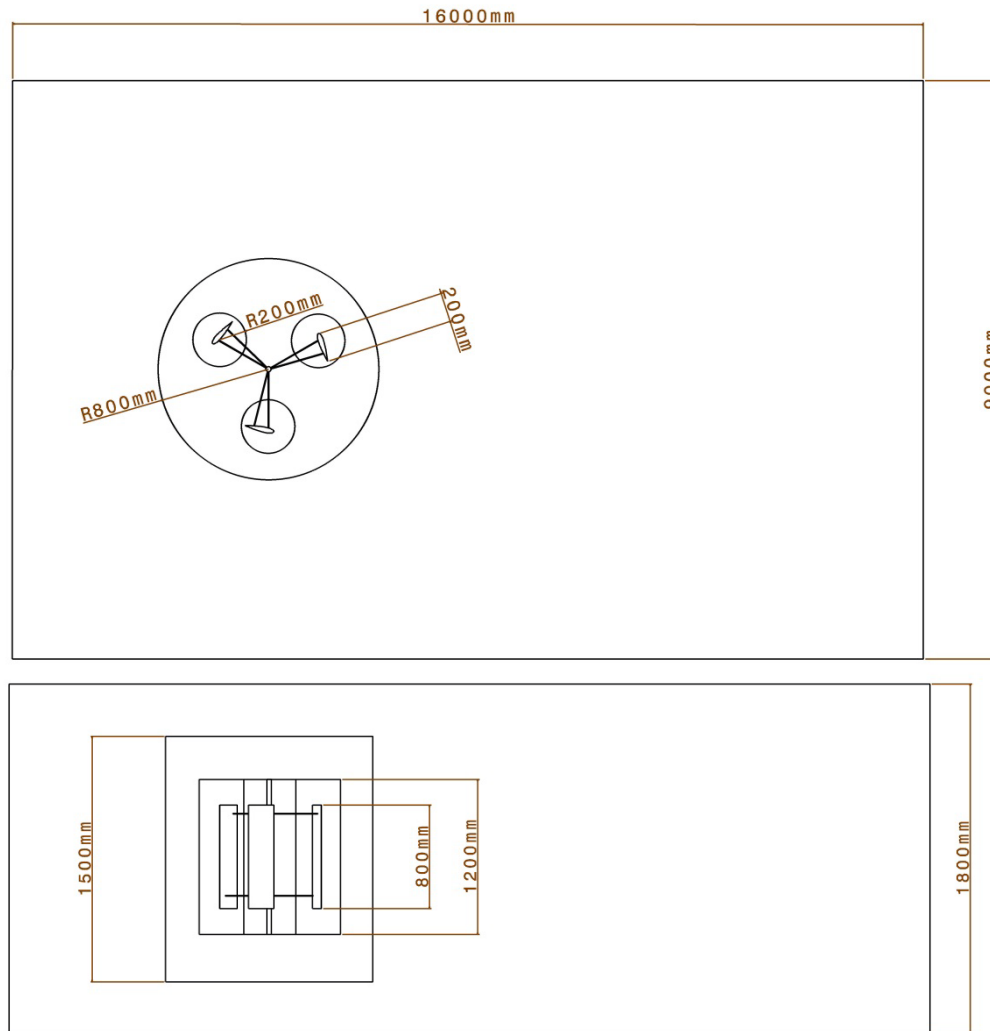Figure 4: Outer, rotor, and blade domains of the VAWT with the specified boundary conditions

Figure 5: Plane views of all three domains with the specified dimensions

3.3 Outer Domain

This fixed domain represents the bulk of the fluid surrounding the VAWT. The dimensions of this domain were carefully considered, in order to allow for sufficient clearances around the VAWT, making sure that there was no interference caused by the boundaries. Thus, the width was chosen to be 11 times the diameter of the rotor. The inlet boundary was placed 3 rotor diameters upstream of the rotor, and the pressure outlet boundary was situated 16 rotor diameters downstream of the rotor. The latter considerations are necessary to provide enough space for the generation of the wake behind the rotor. As for the height of the domain, it was chosen to be more than twice that of the wing span. This again is due

to the fact that we need to provide enough clearance for the produced vortices at the blade's tips, which contribute to the induced drag. Dimensions of the domain that are shown in Fig. 5 however, are not drawn to scale.

As for the boundary conditions, the inlet boundary was assigned an inlet velocity according to the simulated case (6 m/s or 8m/s) and the turbulence intensity was set equal to the experimental value of 0.8 %. Turbulence intensity is set at the inlet boundary and is defined as $I = u'/V_\infty$ which is a ratio of the root mean square of the turbulent velocity fluctuations and the mean Reynolds averaged velocity. The pressure outlet was assigned a value of 0 Pa, which stands for the value of the pressure of air at the exit of the outer domain. The other four boundaries surrounding the VAWT were assigned a symmetry boundary condition. A Boolean operation was carried out to remove cylindrical shape, which represents the rotor domain, from the outer domain. An interface boundary condition was set at these surfaces, to ensure the continuity of fluid flow into the rotor domain. An unstructured tetrahedral relatively coarse mesh was used in this domain as there is no intricate fluid interaction that needs to be monitored. A conformal mapping was necessary at the interface, for the sizing of elements in that region should match the sizing of the elements in the adjacent rotor domain. Otherwise, the convergence of the solution was adversely affected.

3.4 Rotor & Blade Domains

As mentioned earlier, the rotor and blade domains were moving domains. This was necessary in order to simulate the rotation of the VAWT embedded within these two domains. The cylindrical rotor domain contained the shaft and the rods of the turbine. A rotational speed ω was specified around the z-axis for this domain and varied according to the tip speed ratio being studied. An unstructured mesh was chosen as it suits fluid applications with irregular geometries. The mesh was made finer in this region as the influential elements of the VAWT were being approached. The rods and shaft were treated with fine face sizing and inflation layers to accurately capture flow variations within the boundary layer. Furthermore, a no-slip boundary condition was set for all rods and shafts. An interface is assigned at the contact surfaces with the wind tunnel and the blade domains. The blade domains consisted of three cylindrical domains that engulfed the blades. Blade domains were created through Boolean operations by subtracting the three cylinders from the main cylindrical rotor domain. The variable pitch mechanism, in which the blades tend to rotate around two axes, was the main motive behind choosing to

separate the blade domains from the rotor domain. The first rotation was set around the z-axis with a specified rotational speed ω, while the other took place around an axis passing through 25% of its chord length with a pitching angle related to the azimuthal angle as given by Eqns. 1 and 2. These equations were fed into the solver and were necessary in guiding the blades' motion. Thus, it was extremely important to center the blade at 0.25c inside this domain for any error in the placement would yield different angle of attacks than those intended throughout the rotation. In addition, having the three blade domains provided a simpler method to control the grid density and quality in the most important region of the field studied.

The finest unstructured mesh amongst all regions was in this domain. The blades were treated with special sizing functions and inflation layers to accurately resolve near-wall flow strucutres. However, the airfoil's trailing edge provided a more complex geometry and the inflation function adversely affected the quality of the mesh. To remedy this problem, fine sizing functions were used at the edges and faces of the blade. In such a situation, a trade-off problem arises between the quality of the grid and the number of elements that can be conceded without reaching an unrealistic computational time later on. Another interface boundary condition was set at the interface between surfaces of the outer and the rotating domains. Finally, a wall boundary condition was assigned to the faces of the blades.

3.5 Flow Solver

ANSYS Fluent, a commercial CFD solver, was utilized to solve the equations of motion. An unsteady implicit coupled pressure based double precision solver was employed. A second order upwind-based discretization scheme was selected for all flow variables whereas bounded central difference discretization scheme was employed for LES simulations with variable Smagorinsky coefficient. The filtered incompressible Navier-Stokes equations can be summarized by

$$\frac{\partial \overline{u}_i}{\partial x_i} = 0$$

$$\frac{\partial \overline{u}_i}{\partial t} + \frac{\partial}{\partial x_j}\left(\overline{u}_i \overline{u}_j\right) = -\frac{1}{\rho}\frac{\partial \overline{p}}{\partial x_i} + \nu \nabla^2 \overline{u}_i - \frac{\partial \tau_{ij}^S}{\partial x_j} \tag{3}$$

The subgrid scale stress term, τ_{ij}^S is written in terms of eddy viscosity, ν_t as

$$\tau_{ij}^S = 2\nu_t S_{ij} + \frac{1}{3}\tau_{kk}\delta_{ij} \qquad (4)$$

where S_{ij} is the strain rate and ν_t is evaluated using dynamic Smagorinsky model [15]. The second-order interpolation scheme was used to calculate cell-face pressures.

The Modified Menter turbulence model [16] was used initially at the beginning of each simulation for the first two blade rotations, after which LES was set to take over. Acquisition of data started after the elapse of the first three full blade rotations, which was necessary to eliminate any transient effects. Time-averaged solution of flow fields was obtained by averaging flow variables at a sampling interval that is equal to the chosen time step. A maximum of 60 iterations per time step was allowed before the solver proceeded to the next time step; however, about 15 to 20 iterations on average were necessary to converge. A convergence criterion of 1×10^{-3} of scaled residuals of all flow variables was obtained before proceeding to the next time step.

4. Validation of CFD model

4.1 Grid Dependency Study

Mesh density / quality may have a substantial influence on the CFD results. Thus, to ensure grid independent results and yet avoid prohibitive computational cost, simulations were carried out using three different mesh resolutions: coarse, medium, and fine. Solutions were deemed grid independent when negligible difference was achieved in the average power coefficients of at least two consecutive meshes. Comparisons among the forgoing three meshes were made for the NACA 0018 fixed-pitch mechanism at a wind speed of 8m/s and TSR of 1. This case was selected because it relatively requires tolerable computational cost as lower TSRs involve massive flow separation and thus require more iterations per time step to converge. Figure 6 depicts the instantaneous power coefficient versus azimuthal angle for a complete rotation post the transient startup of the turbine.

10 and 16 layers of inflation prisms were placed in the boundary-layer with the first grid node set at y of 3×10^{-6}m and 2.1×10^{-6}m off the surface for the medium and the high density meshes, respectively,

resulting in values of y^+ that close to one on all three blades and connecting mechanisms. These values are further reduced over the first two consecutive rotations using grid adaptation techniques.

A geometric expansion ratio of 1.2 was employed, resulting in prisms that contributed to about 18 and 22 % of the total number of cells for the fixed and variable pitch mechanisms, respectively. The rest of the domain was composed of a combination of pyramids and tetrahedron elements. Table 2 details the grid-resolution study along with corresponding values of y^+ for the considered NACA 0018 test case. For all forthcoming cases, assessments are made based on the results of the finest employed mesh. A top view of the coarse size mesh in which a cut is taken at a chordwise location near mid plane, showing mesh layout and concentration of nodes, is depicted in Fig 7. All values of y^+ reported in table 2 belong to the NACA 0018 test case at a TSR of 1.0.
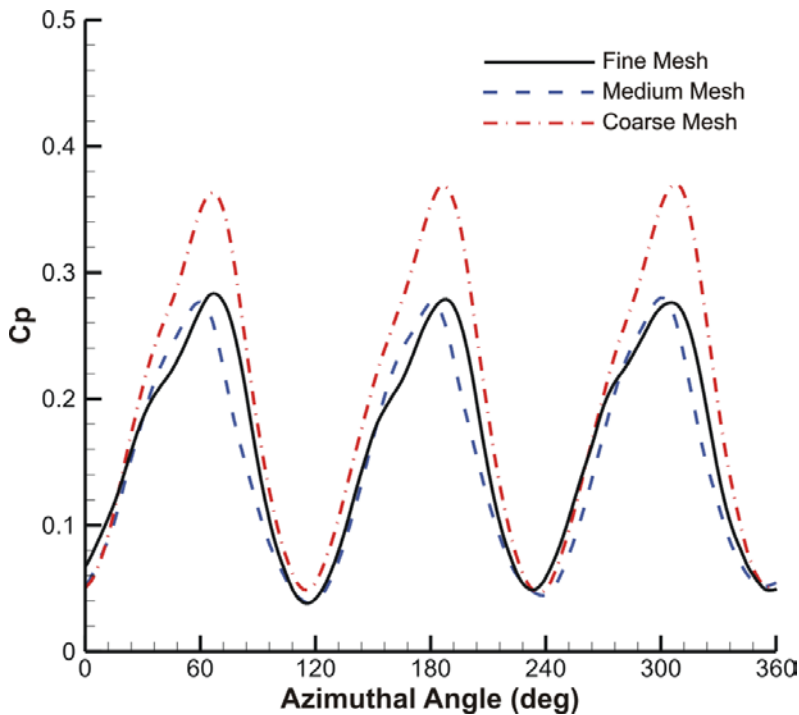

Figure 6: Effect of grid size on the accuracy of the solution at TSR=1.
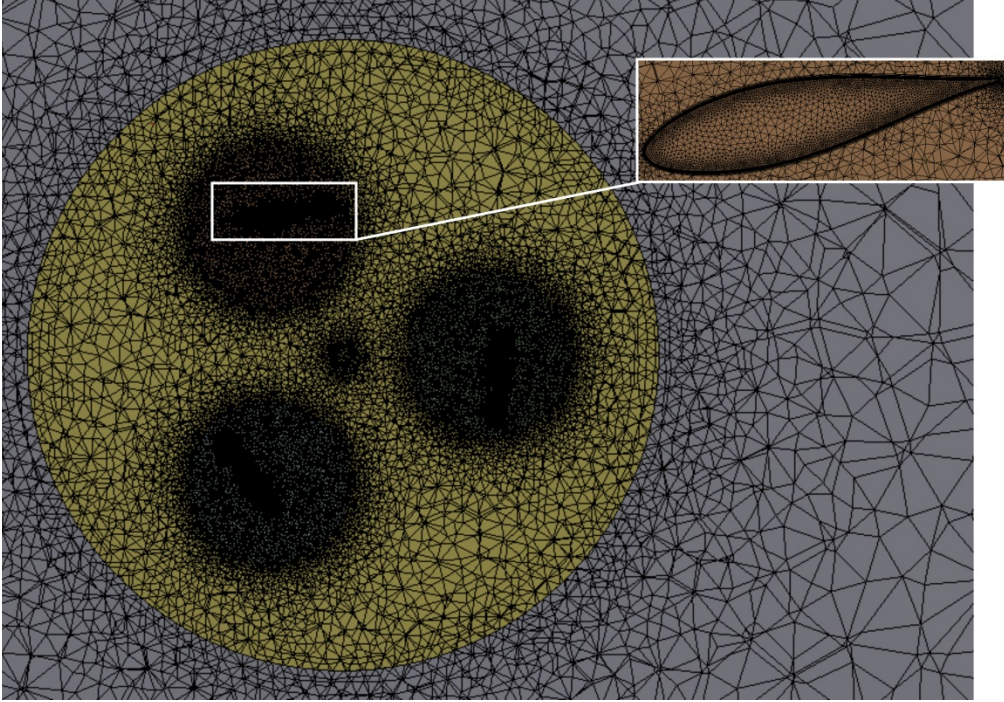
Figure 7: A plane view of the overall domains showing the rotating core of the three-straight blades along with near surface grid clustering.

Table 2: Considered grids for the NACA0018 fixed-pitch mechanism at TSR =1 and incoming wind speed of 8m/s.

Grid	Name	Number of cells ($\times 10^{-6}$)	Model	y^+
1	Coarse	5.647	LES	0.8768
2	Medium	11.960	LES	0.9540
3	Fine	15.371	LES	0.6478

4.2 Time dependency study

Two simulations were carried out in order to determine how the time step affects the turbine power coefficient. The objective is to use a large time step that guarantees the lowest computational time without compromising the accuracy of the results. The study was run for the NACA 0018 with wind speed of 8 m/s at a TSR of 1 at two different time steps corresponding to $\Delta t = 0.00157079$ and $\Delta t = 0.00078535$. These values correspond to the time needed to rotate $2\pi/300$ and $2\pi/600$ respectively. The results of the instantaneous power coefficients are plotted in Fig. 8 for both of these time steps post the transient startup of the turbine. It can be seen that the results are extremely close and thus utilizing the

larger Δt does not decrease the accuracy of the predicted results. Hence, a time step based on $2\pi/300$ degree is adopted for all tip speed ratios throughout the present work.
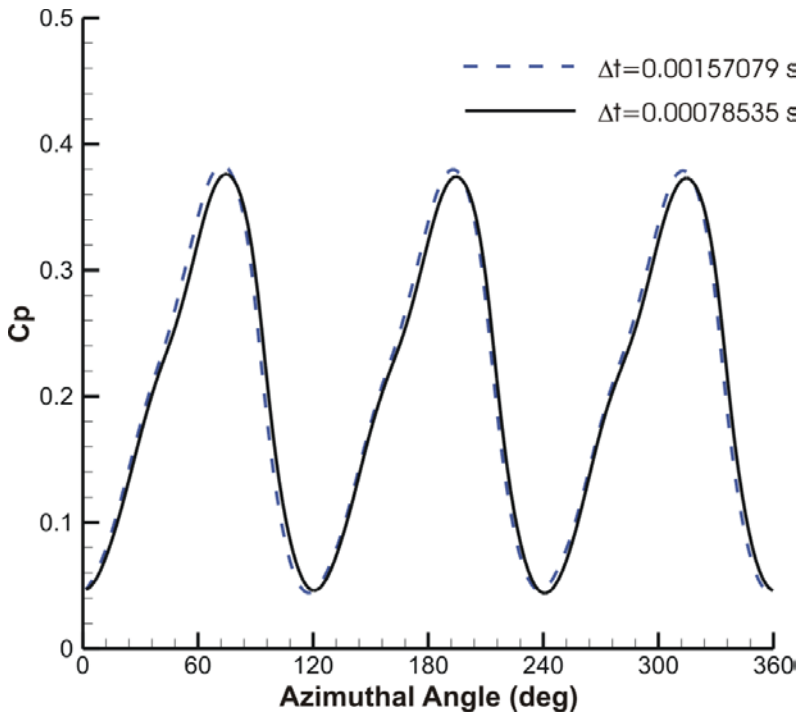

Figure 8: Effect of time step on the accuracy of the solution at TSR=1.

5. Results

The inflow angle of the tail vane (eccentric angle θp) was set to zero in both the experiments and the numerical simulations. The modeling of θp along with equations 1 & 2 were employed in Fluent utilizing the User Defined Scalars/Functions (UDS/UDF). It is worth mentioning that the power coefficient as measured in the experiment includes the power loss due to pitching motion of blades (inertia moment of blades), and excludes the bearings loss of the main shaft. On the contrary, the numerical study accounts only for the losses of the main and the second links.

It should be noted that solidity plays a major role in dictating the TSR at which the turbine reaches its maximum power coefficient. Turbines attaining their maximum efficiency at TSR between 2 and 3 showed maximum power coefficients of less than 30 %. Given the high solidity of the present turbine, as well as its low AR, it is expected that its maximum Cp values to be even lower. Low solidity turbines are conventionally used for low torque, low speed operations whereas high solidity turbines are used for

high torque, low speed operations. The later scenario is of interest in the present design as relatively low velocities minimize vibration response due to turbine imbalance. This in turn maximizes the turbine longevity while producing acceptable power output.

In the following subsections the effects of wind speed, airfoil shape, connecting rods, and incoming turbulent intensity on the performance of the VAWT are assessed. It is worthwhile to mention that only five points at TSRs of 0.25, 0.5, 0.75, 1.0, 1.25, and 1.5 were numerically simulated for each of the considered test cases as the computational cost was substantially excessive. For instance, it took about 38 hrs for the medium density mesh to complete one full rotation using parallel computing of 6 cores on Intel Xeon E5 2.6GHz processors. In the best case scenario, a minimum of five full rotations were necessary to confidently predict a single averaged power coefficient value. These six values are designated by symbols, whereas the experimental data points are connected together via a third order spline function.

5.1 Effect of wind speed

The power coefficient of a VAWT increases with an increase in the tip speed ratio and reaches a peak, after which it takes a dip as larger tip speed ratios are attained. To shed some light on this behavior, the angle of attack is assessed for tip speed ratios of 0.5 and 1.5 as depicted in Fig. 9. It can be clearly evident that the blade throughout its motion concedes much smaller angles of attack at higher tip speed ratios. This in turn causes the blades to generate more lift as they operate for a longer period in the envelope that produces higher lift. On the contrary, at lower tip speed ratios, the blades operate for a longer period at very high angles of attack. Thus stalling occurs, which eventually leads to flow separations and vortices formation that are convected downstream. These vortices interact with the blades downstream and hamper their lift generation. At high tip speed ratios, the role played by the rods becomes more imminent as drag builds up. Consequently, this result in an adverse effect on the power coefficient since lift created in by the blade is desired while the drag of the connecting rods tends to slow down the motion of the turbine.

The effect of freestream velocity on the power coefficient for a fixed-pitch NACA 0018 is shown for a wind speed range of 6-10 m/s in Fig. 10. The predictions of LES compare very favorably with corresponding experimental findings for wind speeds of 6 m/s and 8 m/s. This close agreement clearly indicates that connecting rods are appropriately accounted for in the numerical model. Furthermore, it is

evident that for wind speeds $\geq$ 8m/s results of the experimental data fall very close to each other. It is worth noting that the discrepancy between numerical and experimental data was computed using the Normalized Mean Square Error (NMSE). The maximum error took place at a TSR of 0.5 with values of 1.562 % and 9.387 % for the 6 m/s and 8 m/s, respectively.

The lift generation of the blades depends on the Reynolds number which in turn depends on the speed. To a certain extent, lift generation increases with the increase in Reynolds number. However, the highest power coefficient curve, with a maximum value of 0.21 at a TSR of 1.3, was noticed at the smallest wind speed of 6 m/s. This could be related to the Reynolds number associated with complex flow physics that may well involve laminar separation transition, a scenario encountered by Elkhoury et.al. [10] on a similar test case. URANS models are not capable of capturing this flow feature as they are very dissipative in nature and usually results in over predicting the performance of the turbine. Therefore, as a result of this laminar separation transition it could be deduced that the increase in drag outweighs the increase in lift for NACA0018 airfoil for wind speeds between 8 and 10 m/s, a phenomenon that does not occur at a lower velocity of 6 m/s for this airfoil. A similar behavior however, to a lesser extent is also noticed by the experimental data as depicted in Fig. 11. The largest Cp distribution for the fixed-pitch NACA 63_4-221 blade occurs for the freestream wind speed of 4 m/s after which experimental values collapse very well at 8 m/s and 10 m/s. Given these similarities in Cp distribution at 8 and 10 m/s for the NACA0018 and the NACA 63_4-221 blades, it was deemed numerically cheaper to carry out the simulations at the lower wind speed of 8 m/s. In addition, this wind turbine is intended for urban use and therefore, wind speeds of 10 m/s or above would be rarely encountered.
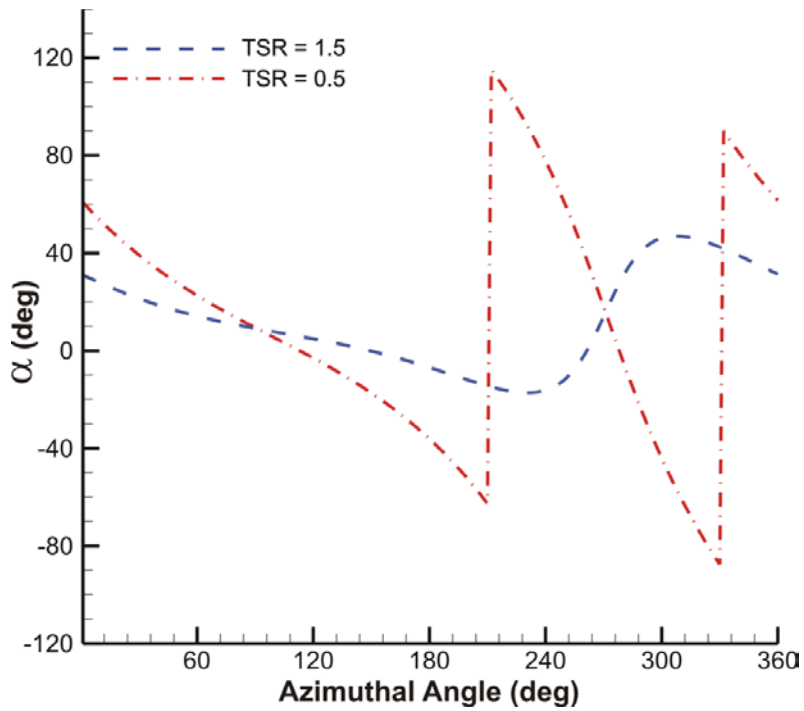
Figure 9: Variation of angle of attack vs azimuthal angle for two tip speed ratios of 0.5 and 1.5 at $\theta_p=0^o$.
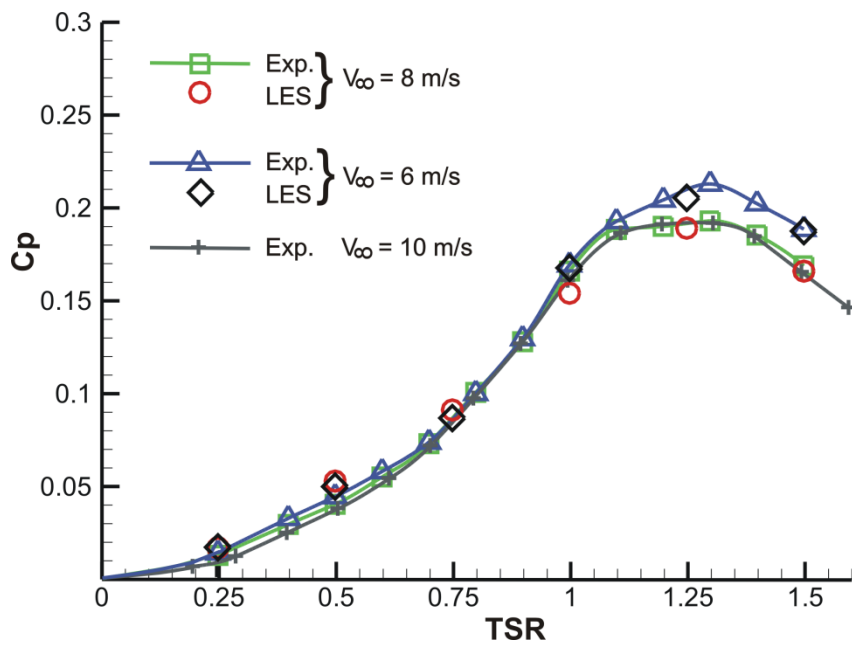

Figure 10: Average power coefficient vs tip speed ratio for a fixed-pitch, NACA 0018, at three different freestream velocities.
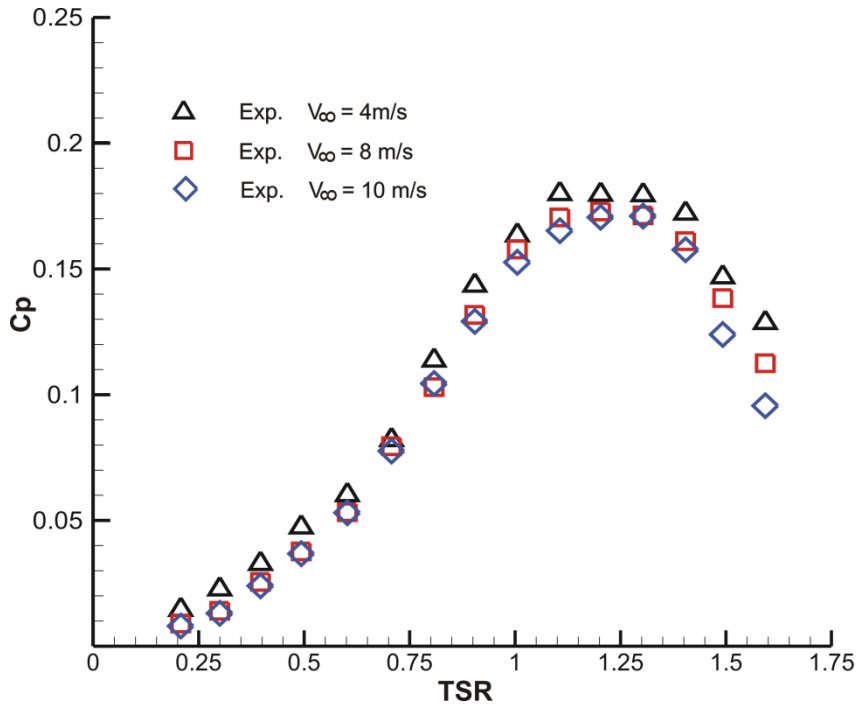
Figure 11: Average power coefficient vs tip speed ratio for a fixed-pitch, NACA 63$_4$-221, at three different freestream velocities.

5.2 Effect of airfoil shape

Thickness and camber of the airfoil were altered in order to assess the influence of these characteristics on the performance of the VAWT. The effect of the former on the power coefficient is depicted in Fig. 12 for the NACA 0018 and the NACA 0021 airfoil sections. The comparison was made on a fixed-pitch mechanism at a wind speed of 8m/s. Aside from the thickness all variables were held the same for both cases. Conventionally, the third and fourth digits of a four digit NACA airfoil resemble the maximum thickness as a percentage of the chord, located at 30% of the chord length measured from the leading edge. Hence, NACA 0021 is 3% thicker than NACA0018. When thickness is increased, the radius of curvature at the leading edge is also increased. This in turn allows for milder changes in pressure leading to better stall characteristics. This is clearly verified by both the experimental and the numerical results as the power coefficient of the NACA 0021 is consistently higher than that of the NACA 0018 for all tip speed ratios. Thinner airfoils tend to perform better when used with lower solidity turbines at high TSRs (>3.0) [5]. Increasing the thickness is usually beneficial for strengthening the blade's structure which is subject to fatigue as the forces acting on it fluctuate during a

complete revolution of the turbine. According to the NMSE, the maximum discrepancy between the computational and the experimental data was found to be 9.22% for the NACA 0018 and 2.04% for the NACA 0021 airfoil at a TSR of 0.5 for both cases.

The camber effect is assessed through the comparison of the symmetric 4-digit NACA 0021 and the laminar cambered 6-digit NACA 63_4-221 airfoils. Both airfoils have a thickness ratio of 21% and were compared with variable-pitch mechanism at an incoming wind speed of 8 m/s. The experimental results of the power coefficient show little difference between the two airfoils as depicted in Fig. 13. The NACA 0021 exhibits a slightly higher Cp values at tip speed ratios between 1.0 and 1.25. The results of the LES are in good agreement with the experiments as they clearly show lower Cp values for the NACA 63_4-221. It is worth noting that the effect of camber did not show any improvement on the self-start of the turbine. The maximum NMSE between the computational and the experimental data was found to be 10.15% for the NACA 0021 and 7.81 % for the NACA 63_4-221 airfoil, both of which occurred at a TSR of 1.5.
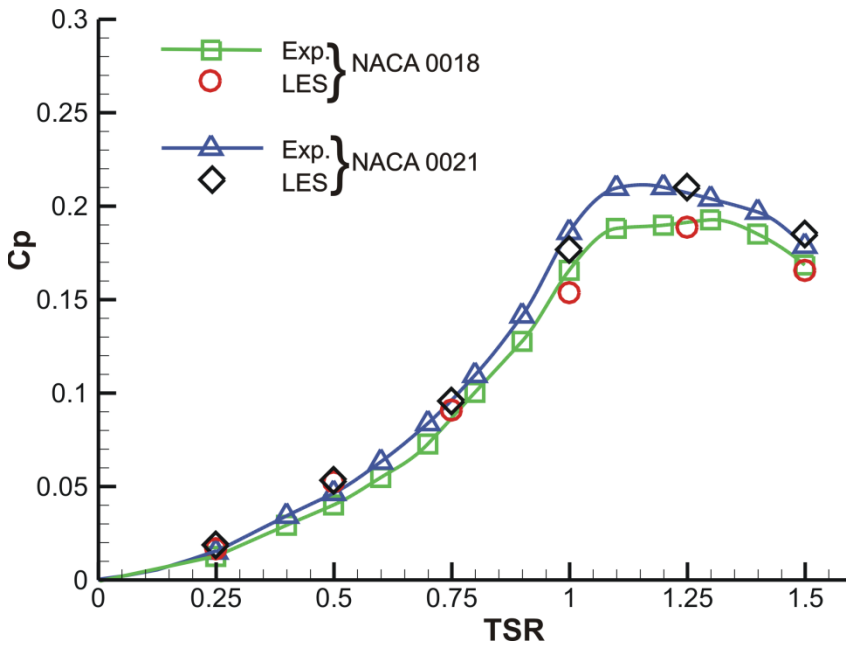

Figure 12: Average power coefficient vs tip speed ratio for a fixed-pitch-angle, NACA 0018, and NACA 0021, at a freestream velocity of 8m/s.
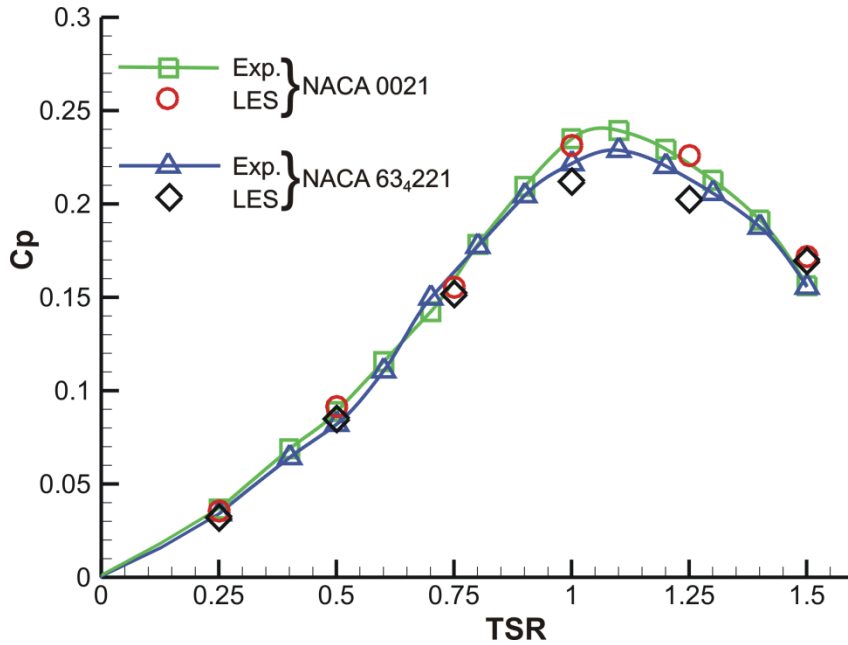
Figure 13: Average power coefficient vs tip speed ratio for a variable-pitch-angle, NACA 0021, and NACA 63$_4$-221, at a freestream velocity of 8m/s

5.3 Blade vortex interaction

Complex flow structures evolve around the blades of a VAWT undergoing dynamic stall at high angles of attack and low TSR. Dynamic stall is characterized by large recirculation separated flow regions with the formation of vorticies that are shed downstream and may impinge on other rotating blades in the downwind half as will be depicted shortly. As a result of this blade vortex interaction, this turbine produces power at low TSR, a trait that is missing in turbines with low solidity. This serves as another motive behind the selection of present turbine.

To shed some light on the complex flow structures associated with low TSRs, consider the vorticity contours on a plane that cuts mid through the turbine blades of a variable-pitch with NACA 63$_4$-22 at TSR = 0.5 as shown in Fig. 14. Not only interaction of flow structures can be notice at this low TSR but also the various stages involved through dynamic stall at different azimuth angles. Attached flow is observed between an azimuthal angle of 90º and 160º. Leading edge vortex begins to roll up around ϕ = 170º and continues to grow while remaining intact until 240º. For this range of azimuthal angles, the trailing edge vortex gets detached at first and convected downstream. Afterwards, an elongated vortex forms and rolls towards the surface of the blade as can be observed at ϕ =225º in Fig. 14. Then the

leading edge vortex breaks up into small patches as a result of the leading/ trailing edge vortex interaction which can be clearly noticed at $\phi = 270^o$ in Fig. 14. At $\phi = 290^o$ the formation of a new leading and trailing edge vorticies are observed. The trailing edge vortex detaches around $\phi = 0^o$ and gets convected downstream. Again, an elongated vortex forms at the leading edge and rolls up towards the surface of the blade as can be observed at $\phi = 345^o$ in Fig. 14. The interaction between these two vorticies takes place around $\phi = 20^o$ and starts to form negative and positive concentrated patches that are well noticed at 30°. At $\phi = 65^o$ the trailing edge vortex gets shed downstream and a new vortex begins to develop and expand along with the leading edge vortex. A large scale vortex interaction is observed between an azimuthal angle of 60° and 90°. Finally, the flow reattaches to the blade surface and the same vortex dynamics starts over in a new cycle.

Considering the selected instantaneous vorticity fields depicted in Fig. 14, it is evident that all wakes generated by the blades located upwind ($90^o <\phi <270^o$) are convected towards the top right quarter. These flow structures not only interact with the blades but also with the shaft (as seen to the right of the figure) to degenerate into unsteady vortices.
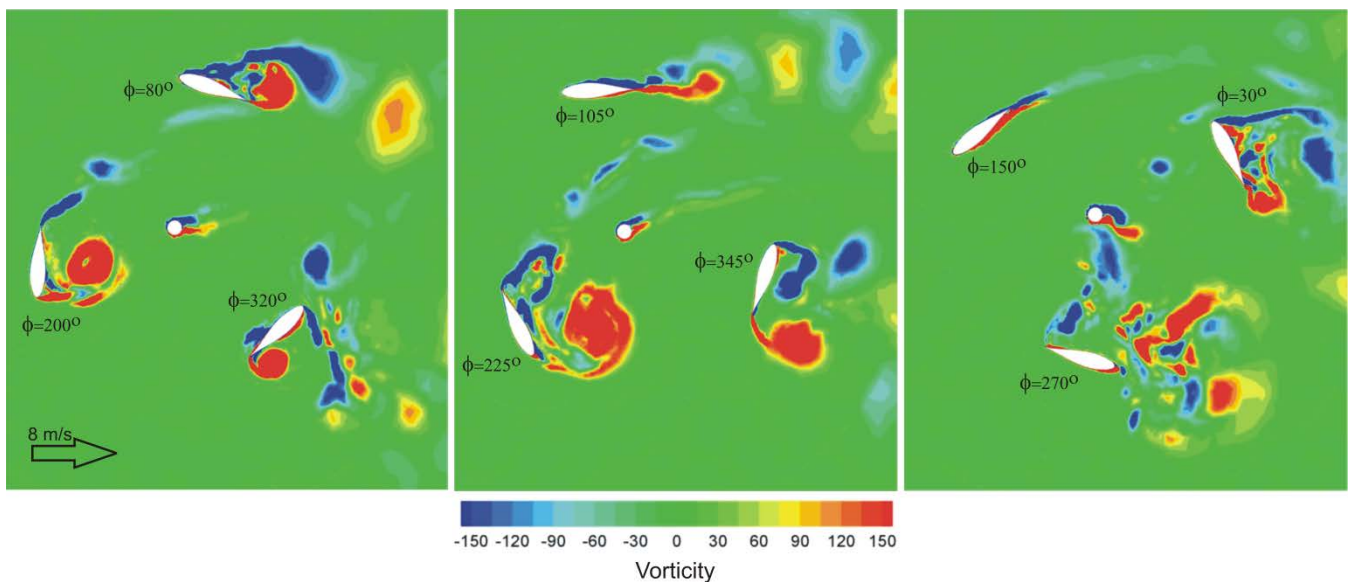

Figure 14: Instantaneous vorticity field on a mid-plane of a variable-pitch-angle VAWT, with NACA 63_4-221, at $\text{TSR} = 0.5$, showing different azimuthal angles ϕ.

5.4 Effect of variable-pitch

The effect of variable-pitch on the performance of the VAWT is assessed against that of the fixed-pitch mechanism. The variation in the angle of attack with azimuthal position for fixed- and variable-pitch turbine as well as the adjustment made by the variable-pitch mechanism is depicted in Fig. 15. Moreover, the adjustment made by the variable-pitch mechanism modifies the angle of attack in order to fit into an envelope that enhances the lift, and thus the generated power. A comparison of power coefficient vs TSR between fixed- and variable-pitch is depicted in Fig. 16. The utilized airfoil of the considered VAWT is the NACA 0018 at a wind speed of 8m/s. The power coefficient at all TSRs below 1.5 shows significant increase with variable-pitch mechanism. However, the peak in the power coefficient takes place at a lower TSR than that of the fixed-pitch, suggesting that the losses due to the moving mechanism is larger than that of the fixed, and is evident by the steep decrease in Cp values for TSRs >1.1. LES predicts the same remarkable increase in the power coefficients and matches to a large extent the experimental data with a slightly under predicted value at $TSR=1.0$, inferring that sliding mesh approach is sufficiently accurate to model a high solidity VAWT with variable-pitch mechanism. Thus, the maximum NMSE was 8.856% for the fixed-pitch and 9.61% for the variable-pitch at TSRs of 0.5 and 0.75, respectively.

Instantaneous contours of pressure coefficient on a plane that cuts midway through the VAWT are shown in Fig.17. These contours are compared for fixed- and variable-pitch NACA 0018 turbine at TSR $=1.0$. This TSR was chosen for it belongs to a location at which large difference in power coefficient between fixed- and variable-pitch is observed. A comparison between fixed- and variable-pitch blade orientations is shown in the left side of Fig.17. This slight orientation difference is sufficient to cause larger areas of negative pressure coefficient around the blades as opposed to those observed with the fixed-pitch shown in the right side of Fig. 17. The increase in the power coefficient of the variable-pitch VAWT is, to a large extent, due to this rise in negative pressure coefficient.

Another test case of a fixed- vs variable-pitch mechanism, however, for a thicker NACA 0021 airfoil is shown in Fig. 18. Again as was the case with the NACA 0018, the power coefficient of the variable-pitch is higher than that of the fixed-pitch with a peak that occurred slightly earlier, however, drops to a lower value than that of the fixed-pitch at TSR >1.35. A quick comparison between both considered variable-pitch airfoils reveals that the VAWT with the thinner airfoil achieves a higher C_{PMAX} value and continues to have a higher aerodynamic performance at high TSRs past C_{PMAX}. Thinner airfoils tend to

perform better because the proposed variable-pitch mechanism improves flow characteristics by reducing the time during which the blade stalls. It is worth noting that the effect of variable-pitch mechanism had a positive influence on the self-start of the turbine, where the self-start velocity dropped from 3 m/s for the fixed- to 2.5 m/s for the variable-pitch mechanism. Comparisons between experimental and computational data reveal a maximum NMSE of 8.81% for the fixed-pitch and1.05 % for the variable-pitch at TSRs of 0.25 and 1.5, respectively.
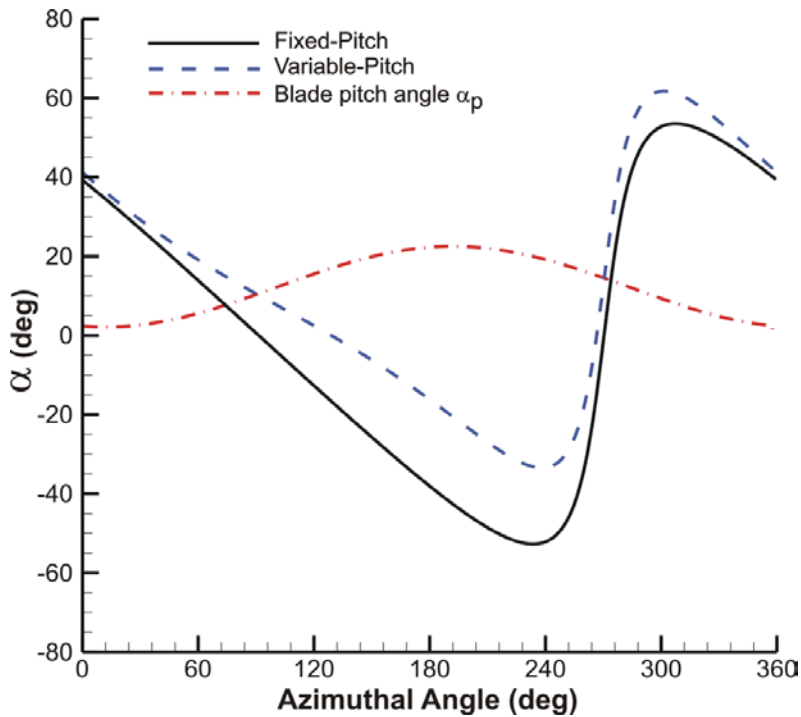

Figure 15: Variation of angle of attack vs azimuthal angle for a tip speed ratio of 1.5, $\alpha_c = 12^\circ$, $\alpha_w = \pm 10^\circ$, and $\theta_p = 0^\circ$.
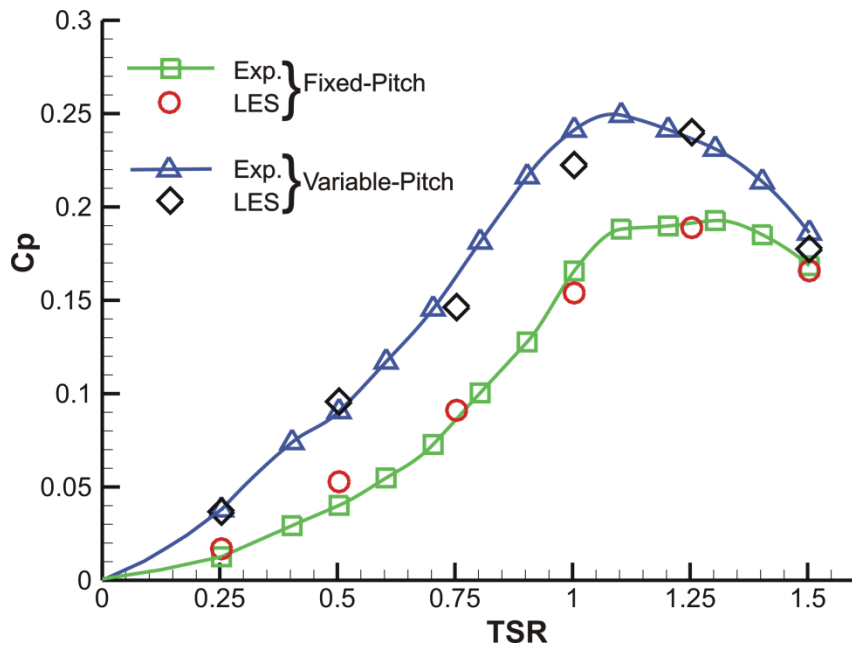
Figure 16: Average power coefficient vs tip speed ratio for a fixed- and a variable-pitch-angle, NACA 0018, at a freestream velocity of 8m/s.
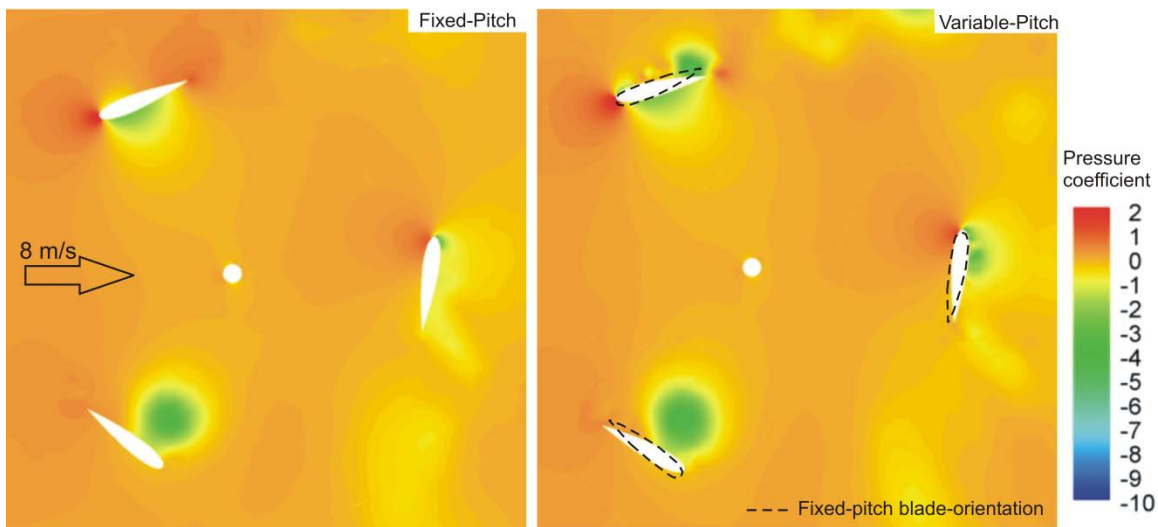

Figure 17: Instantaneous pressure coefficient through mid-plane of a fixed- and variable-pitch angle VAWT, with NACA 0018, at $TSR = 1.0$.
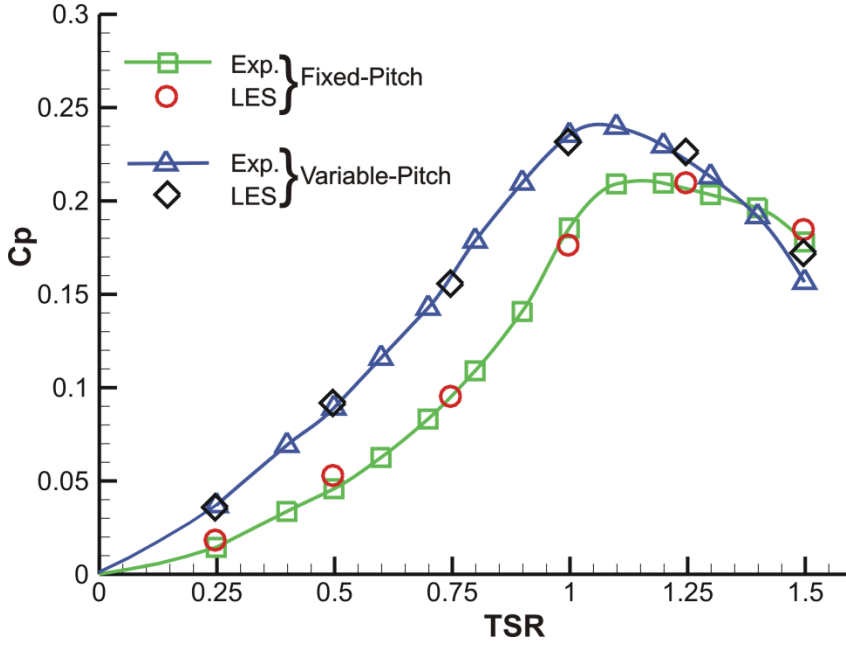
Figure 18: Average power coefficient vs tip speed ratio for a fixed- and a variable-pitch-angle, NACA 0021, at a freestream velocity of 8m/s.

5.5 Effect of connecting rods

The NACA 0018 airfoil at a wind speed of 8m/s was used to assess the impact of connecting rods on the performance of the VAWT. The power coefficient of a fixed-pitch mechanism with nine connecting rods along vs a rod-free three-blade turbine is depicted in Fig. 19. The effect of strut drag and shaft interference has a great influence on Cp with increasing TSR, and becomes more important at TSRs > 1.0. The influence of the rods on the power coefficient as a function of TSR could be better understood by plotting the difference of the two Cp curves of Fig. 19. Another analytical/empirical solution to quantify the contribution of rods could be approximated utilizing the following drag coefficient equation for cylinders [41], which is valid up to the drag crisis $\text{Re}_D \approx 250,000$

$$C_{d_{rod}} \approx 1 + 10/\text{Re}_D^{2/3}$$

(5)

The velocity at which the Re_D is evaluated is the normal velocity relative to a rod, which is based on the average rigid body rotation of a rod $(\omega R / 2)$ and upstream velocity component $V_{rod} = \omega R / 2 + V_\infty \sin \phi$. The

contribution of Eq. 5 is directly added to or subtracted from the power coefficient based on the sign of $\omega R / 2 + V_\infty \sin \phi$. The loss due to connecting rods, hereafter referred to as Cp_{loss}, is depicted in Fig. 20 for both of approaches. The discrepancy between both solutions is mostly due to strut interference that the analytical/empirical approach does not account for. It is obvious that any attempt at modeling the present VAWT without accounting for rods renders the solution inaccurate.

Contours of vorticity field on a plane that cuts through the upper connecting rods for fixed-pitch NACA 0018 are shown in the left side of Fig. 21, while the right side is for a rod-free simulation at TSR $=1.5$. By close inspection of Fig. 21, it is clearly evident that strut blade interference is not substantial as vorticity field adjacent to turbine blades is minimally affected by the presence of the rods. Therefore, 3-D numerical simulations with variable-pitch mechanism could be carried out without physically modeling the connecting mechanisms that could be accounted for analytically using Eq. 5. It is worth noting that strut blade interference is present at low TSR however, this effect could be neglected as shown in Fig. 19. At this high TSR, static stall is apparent by the presence of amplified vorticity contours adjacent to the surface of the blades. These vortices are shed behind forming a wake structure that is caught by the following blade, an interaction that is clearly seen in both vorticity fields of Fig. 21.
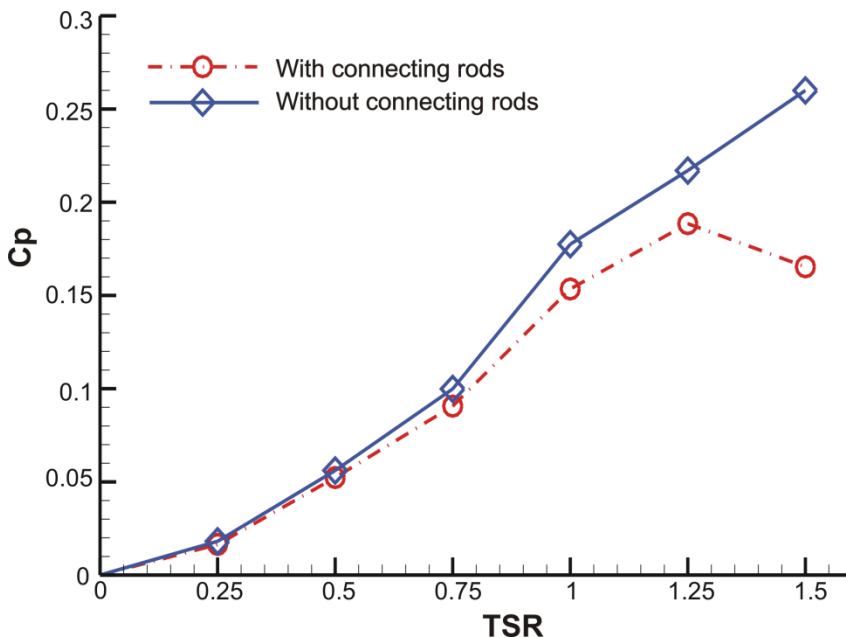

Figure 19: Average power coefficient vs tip speed ratio for a fixed-pitch-angle, NACA 0018, with and without connecting rods, at a freestream velocity of 8m/s.
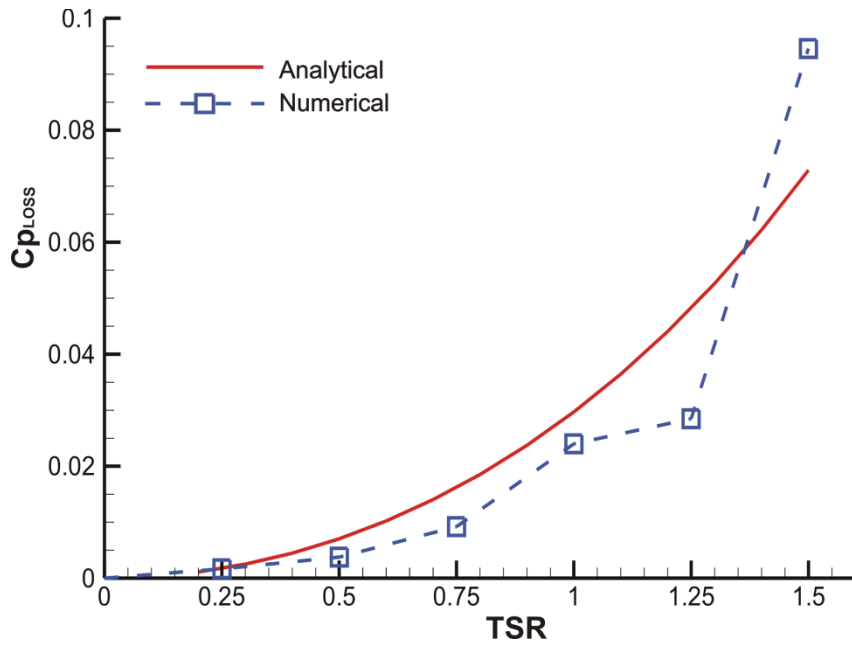
Figure 20: Losses in power coefficient due to connecting rods for the fixed-pitch NACA 0018 airfoil at a freestream velocity of 8 m/s.
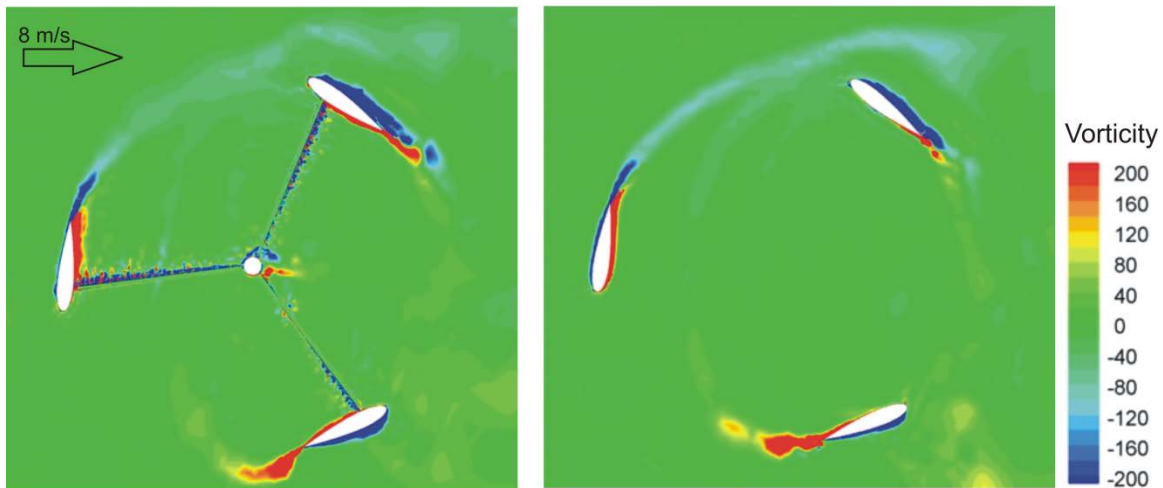

Figure 21: Instantaneous vorticity field on a plane that cuts through the upper rods of a fixed-pitch-angle VAWT, with NACA 0018, at $TSR = 1.0$, showing the effect of connecting mechanisms.

5.6 Effect of incoming turbulence

As the experiments were carried out at a low turbulence intensity level of 0.8%, velocity fluctuations at the inlet boundary condition were neglected, and thus it was assumed that instantaneous velocity components are set equal to their mean velocity equivalents. In order to rule out the effect of time-dependent inlet velocity fluctuations on the solution, the vortex method [17] was used where turbulence is imposed via 2-D perturbations that are added to the inlet mean velocity profile. The previously solved fixed-pitch VAWT with NACA 0018 airfoil and incoming wind speed of 8m/s was chosen to carry out this comparison.

A turbulence intensity level of 0.8% as specified in the experiment was set at the inlet with 190 specified vorticies .These vorticies are formed through particle discretization and convected randomly downstream. Turbulent length scale of 0.0028m was specified according to $l = 0.07 D_h$, where D_h is the hydraulic diameter of the honeycomb openings of the settling chamber in the wind tunnel. As depicted in Fig. 22, LES results showed almost no difference in the power coefficients between the two simulations. This is due to the fact that the vortices created at the inlet would have died out by the time they reach the turbine. Therefore, such a low level of turbulence at the inlet with or without imposed perturbations has not effect on the predicted LES results.
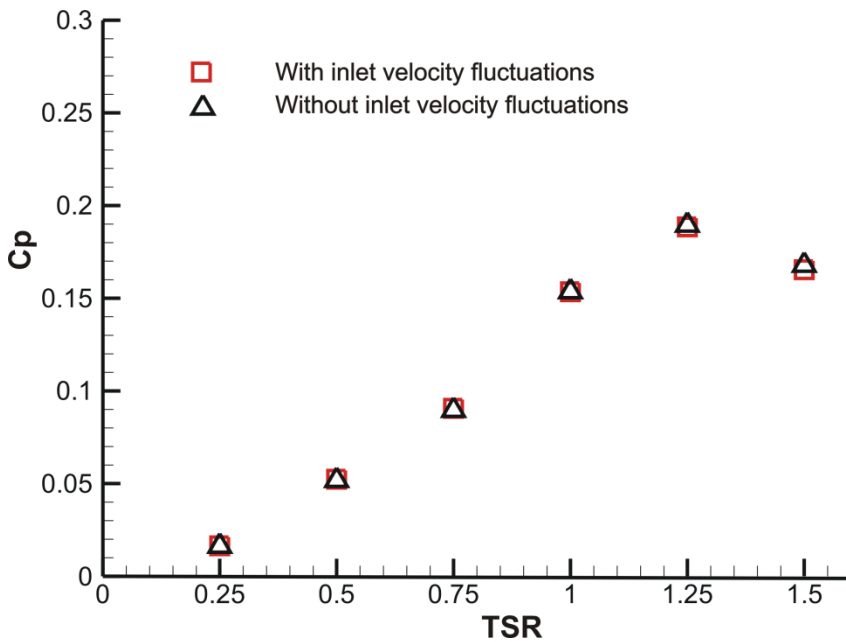

Figure 22: Average power coefficient vs tip speed ratio for a fixed-pitch-angle, NACA 0018, at a freestream velocity of 8m/s, and various inlet boundary conditions.

6   Concluding Remarks

Wind tunnel experiments accompanied by LES were successfully carried out for a VAWT with variable-pitch straight blades to assess the effect of wind speed, airfoil shape, and variable-pitch mechanism on the performance of turbine. Understanding the impact of these parameters is crucial and should be employed in futures ventures to improve the functionality of VAWTs. Major findings emerging from the study may be summarized as follows:

a) LES with dynamic Smagorinski coefficient was able to accurately predict the performance of VAWT with fixed- and variable-pitch mechanism. The sliding mesh technique was used in the modeling of the variable-pitch mechanism. Although some eccentric links *lc* and *le* were not modeled along with the inertial effect of the blades, the approach deemed to be sufficiently accurate with a maximum NMSE of 10.15 %. In the majority of the cases, the maximum NMSE was noticed either at a low TSR or at a high TSR. This in turn reflects the challenges of accurately capturing complex flow physics associated with dynamic stall at low TSRs as well as correctly accounting for the connecting mechanism at high TSRs.

b) Experimental and numerical findings revealed that thicker airfoils tend to perform better for the considered fixed-pitch VAWT with high solidity ratio. This is mainly due to the better stall characteristics thicker airfoils inherit. The NACA 0021 and NACA 63_4-221 airfoils were compared to assess the effect of camber on the performance of the turbine. It was found that the symmetric airfoil had a slightly better performance at TSRs corresponding to highest *Cp* values without a noticeable effect on the self-start of the VAWT.

c) The considered four-bar-linkage variable-pitch mechanism showed superior performance compared to its counterpart fixed-pitch VAWT. Unlike with the fixed-pitch mechanism, the thinner airfoil, NACA 0018, resulted in better performance than that obtained with the NACA 0021 at high TSR > 1.0. This was attributed to the benign envelope of angles of attack within which the variable-pitch mechanism operates. The self-start of the VAWT with variable-pitch mechanism exhibited a lower start-up speed compare to that of the fixed-pitch turbine.

d) It was found that the contribution of the connecting rods can only be neglected at low TSRs as their impact on the power coefficient increases exponentially with increasing TSR. Furthermore, blade strut interaction was found to be minimal at high TSRs. This in turn alleviates the necessity to model complex strut mechanisms by accounting for their contribution using analytical approaches. The effect on incoming turbulence manifested by imposed velocity fluctuations on the mean velocity components at the inlet was assessed. Results were insensitive to inlet velocity perturbations provided that experimental turbulence intensity and length scale values were not altered.

e) Highest power coefficient distribution curves were noticed in the experiments at low wind speeds of 6 m/s and 4 m/s for the fixed-pitch NACA0018 and NACA 63_4-221 airfoils, respectively, after which experimental values collapse very well for higher wind speeds. This is thought to be related to the complex flow physics that may involve laminar separation transition at relevant Reynolds numbers, a point that deserves further investigation in future studies. LES with dynamic Smagorinski was capable of capturing this variation in the power coefficient.

Nomenclature

AR	: Aspect ratio of blade ($= h/c$)
C_d	: Drag coefficient
C_p	: Turbine power coefficient ($= T\omega /\rho RhV^3$)
C_{PMAX}	: Maximum pressure coefficient
c	: Blade chord length
D	: Turbine diameter
D_h	: Hydraulic diameter
h	: Blade span length
I	: Turbulence intensity ($= u'/V_\infty$)
l	: Turbulent length scale
l_c	: Blade link length
l_e	: Eccentric link length
l_m	: Main link length
l_s	: Second link length
N	: Turbine rotational speed
n	: Number of blades
$\overline{p}$	: Filtered pressure
R	: Turbine radius
Re	: Reynolds number
S_{ii}	: Strain rate tensor
T	: Turbine torque
TSR	: Tip speed ratio ($= R\omega / V_\infty$)
u'	: Root mean square of the turbulent velocity fluctuation
$\overline{u}_i$	: Filtered velocity component
V_∞	: Wind speed
y^+	: Dimensionless wall distance
α	: Geometrical angle of attack
α_c	: Blade offset pitch angle
α_p	: Blade pitch angle
α_w	: Blade pitch angle amplitude
Φ	: Azimuth angle (angle between the main-link and x-axis)
θ_p	: Eccentric angle (angle between the eccentric link and x-axis)
ρ	: Air density
σ	: Turbine solidity ($= nc/2\pi R$)
ν	: Laminar kinematic viscosity
ν_τ	: Subgrid turbulent viscosity
τ_{ii}^S	: Subgrid scale stress tensor
ω	: Turbine angular velocity ($= 2\pi N/60$)

References

[1] Mertens S., Wind energy in the built environment: Concentrator effects of buildings (TU Delft) 2006.

[2] Ferreira C. J.,van Bussel G, vanKuik G. A 2D CFD simulation of dynamic stall on a vertical axis wind turbine: verification and validation with PIV measurements. Proceedings of the 45th AIAA Aerospace Sciences Meeting and Exhibit, American Institute of Aeronautics and Astronautics, 2007, pp.1–11.

[3] Hofemann C, Ferreira C J, Van Bussel, G J, Van Kuik G A, Scarano F, Dixon,K R. 3-D Stereo PIV Study of Tip Vortex Evolution on a VAWT. European Wind Energy Association EWEA. 2008, pp.1–8.

[4] Stankovic S, Campbell N, Harries A. Urban Wind Energy Earthscan. 2009.

[5] Dai Y, and Lam W. Numerical Study of Straight-Bladed Darrieus-Type Tidal Turbine. *ICE-Energy*, 2009, Vol. 162, pp.67–76.

[6] Lain S. Simulation and Evaluation of a Straight-Bladed Darrieus-Type Cross Flow Marine Turbine. *Journal of Scientific and Industrial Research*, 2010, Vol. 69, pp.906-912.

[7] Danao L A, Edwards J, Eboibi O, Howell R. A numerical investigation into the influence of unsteady wind on the performance and aerodynamics of a vertical axis wind turbine. *Applied Energy*, 2014, Vol.116, pp. 111-124.

[8] Almohammadi K M, Ingham D B, Ma L, Pourkashan M. Computational fluid dynamics (CFD) mesh independency techniques for a straight blade vertical axis wind turbine. *Energy*, 2013, Vol. 58, pp. 483-493.

[9] Nobile R, Vahdati M, Barlow J F, Mewburn-Crook A. Unsteady flow simulation of a vertical axis augmented wind turbine: A two-dimensional study. *Journal of Wind Engineering and Industrial Aerodynamics*, 2014, Vol. 125, pp. 168-179.

[10] Elkhoury M, Kiwata T, Issa J. Aerodynamic Loads Predictions of a Vertical-Axis Wind Turbine Utilizing Various Turbulence Closures. 12th International Symposium on Fluid Control, Measurement and Visualization, 2013, Nov 18-23, Nara, Japan. pp. 1-9.

[11] Lanzafame R, Mauro S, Messina M. 2D CFD Modeling of H-Darrieus Wind Turbines using a Transition Turbulence Model. *Energy Procedia*, 2014, Vol. 45, pp.131-140.

[12] Menter F R, Langtry R B, Likki S R, Suzen Y B, Huang P G, Volker S. A Correlation-Based Transition Model using Local Variables- Part I: Model Formulation. *ASME Journal of Turbomachinery*, 2006, Vol. 128, pp. 413-422.

[13] Scheurich F, Brown R E. Modelling the aerodynamics of vertical-axis wind turbines in unsteady wind conditions," *Wind Energy*, 2013, Vol. 16, Issue 1, pp. 91-107.

[14] McLaren K, Tullis S, Ziada S. Computational fluid dynamics simulation of the aerodynamics of a high solidity, small-scale vertical axis wind turbine. *Wind Energy*, 2012, Vol. 15, Issue 3, pp. 349-361.

[15] Germano M, Piomell, U, Moin P,. Cabot W. A Dynamic Subgrid-Scale Eddy Viscosity Model. *Physics of Fluids A*, 1991, Vol. 3, pp.1760-1765.

[16] Elkhoury M. Modified Menter Model in Comparison with Recently Developed Single-Equation Turbulence Closures. *AIAA Journal,* 2011,Vol. 49, No. 7, pp. 1399-1408.

[17] Mathey F, Cokljat D, Bertoglio J P, Sergent E. Specification of LES Inlet Boundary Condition Using Vortex Method. In K. Hanjalić, Y. Nagano, and M. Tummers, editors 4th International Symposium on Turbulence, Heat and Mass Transfer, Antalya, Turkey. Begell House, Inc. 2003.